Facile fabrication of high-performance thermochromic VO_2-based films on Si for application in phase-change devices

A.J. Santos[a,b,c,*], N. Martin[c], J.J. Jiménez[a,b], R. Alcántara[a,d], S. Margueron[c], A. Casas-Acuña[a,b], R. García[a,b], F. M. Morales[a,b]

[a] *IMEYMAT: Institute of Research on Electron Microscopy and Materials of the University of Cádiz, E-11510, Puerto Real, Spain.*

[b] *Department of Materials Science and Metallurgic Engineering, and Inorganic Chemistry, Faculty of Sciences, University of Cádiz, E-11510 Puerto Real, Spain.*

[c] *Université de Franche-Comté, CNRS, Institut FEMTO-ST, F-25000 Besançon, France.*

[d] *Department of Physical Chemistry, Faculty of Sciences, University of Cádiz, E-11510 Puerto Real, Spain.*

* Corresponding author: antonio.santos@uca.es

Abstract: This work reports on an alternative and advantageous procedure to attain VO_2-based thermochromic coatings on silicon substrates which involves the sputtering of vanadium thin films at glancing angles and their subsequent fast annealing in air atmosphere. By adjusting the thickness/porosity of the vanadium films as well as the thermal treatment parameters, high VO_2(M) yields were achieved for 100, 200 and 300 nm thick layers treated at 475 and 550°C for reaction times below 120 s. Comprehensive structural and compositional characterizations by Raman spectroscopy, X-ray diffraction and scanning-transmission electron microscopies combined with analytical techniques such as electron energy-loss spectroscopy allowed to evidence the successful synthesis of VO_2(M) + V_2O_3/V_6O_{13}/V_2O_5 mixtures. Likewise, a 200 nm thick coating consisting exclusively of VO_2(M) was also achieved. Conversely, the functional characterization of these samples was addressed by variable temperature spectral reflectance and resistivity measurements. The best results were obtained for the VO_2/Si sample, which experienced changes in reflectance of 30–65% in the near-infrared at temperatures between 25ºC and 110ºC. Similarly, it was also proven that the achieved mixtures of vanadium oxides can be advantageous for certain optical applications in specific infrared windows. Finally, the features of the different structural, optical and electrical hysteresis loops associated with the metal-insulator transition of the VO_2/Si sample were disclosed and compared. The remarkable thermochromic performances hereby accomplished highlight the suitability of these VO_2-based coatings for applications in a wide range of optical, optoelectronic and/or electronic smart devices.

Keywords: VO_2 thin films; glancing angle deposition; rapid thermal annealing; metal-to-insulator transition; thermochromism; smart devices.

1. Introduction

Since its discovery in 1959, vanadium dioxide (VO_2) has been one of the most extensively studied functional materials mainly because it undergoes a reversible metal-to-insulator transition (MIT) at temperatures close to 68ºC[1]. Driven by structural changes from insulating monoclinic (M) at low temperature to metallic rutile (R) at temperatures above the transition temperature (T_c), this phenomenon involves great optical and electronic changes, which makes this material especially advantageous for thermochromic smart window applications[2–7]. These appealing properties of VO_2 have also been exploited for a wide range of photonic, optoelectronic and electronic phase-change devices on silicon platforms, such as optical modulators and limiters[8–13], infrared (IR) photodetectors[14,15] or optical[16,17] and electrical[18–21] switches. Likewise, the VO_2/Si system is also considered a potential candidate for its application as a passive intelligent radiator for spacecraft thermal control[22]. However, the cost-effective attainment of VO_2 films remains a challenge due, among other reasons, to its very narrow experimental synthesis window resulting from the complexity of the vanadium-oxygen system (e.g. existence of numerous and more thermodynamically stable oxides, different polymorphs for the same vanadium oxide, etc.), which generally translates into the formation of vanadium oxide mixtures[23–26].

On the other hand, the characteristics of such a MIT transition (critical temperature, order of magnitude, hysteresis width) also depend on other factors such as film thickness[27,28], employed substrate[29,30], grain size distribution and boundaries[31,32], or crystallinity level[33,34], so the choice of one or another synthesis strategy becomes a decisive issue. Several one-step deposition techniques have been implemented to achieve VO_2 nanostructures[28,35–37]. Note that these procedures have obvious difficulties associated with finely controlling fluxes of O_2, N_2

and Ar, as well as with maintaining the required high temperatures (> 450ºC) for long times. A widespread practice today to obtain high quality VO_2 films involves post-deposition annealing steps in air atmosphere. The most commonly used precursors for this two-step approach are metallic vanadium[38–40] and vanadium nitride[41,42].

Within this framework, our previous study introduced an original two-step approach to synthesize VO_2(M) on silicon substrates by means of the hot oxidation of porous vanadium films in air atmosphere[43]. Thanks to the fabrication of vanadium nanostructures with high surface-to-volume area using the GLancing Angle Deposition (GLAD) technique combined with the subsequent implementation of fast and finely controlled thermal treatments, the selective synthesis of vanadium dioxide thicknesses (between 100–400 nm) with controlled grain sizes was accomplished. Nevertheless, the total layer thicknesses addressed in that work (~600 nm) did not allow the fabrication of pure VO_2 coatings, since, before all the remaining vanadium was completely oxidized, the dioxide formed was almost instantly transformed into other more oxygen-enriched oxides, such as V_2O_5. This resulted in maximum VO_2 yields of 70% of the total coating thickness. In addition, this study also lacked comprehensive structural/functional characterizations at variable temperatures, which are necessary to explore the MIT features of the resulting coatings.

In order to fill this gap, this works reports on the rapid air oxidation of porous vanadium films sputtered on silicon substrates from a more global perspective, assessing not only the effect of the different parameters involved in the annealing processes, but also the influence of the layer thickness. With the ultimate aim of attaining pure VO_2/Si films, direct current (DC) magnetron-sputtered V-GLAD layers of 100, 200 and 300 nm nominal thickness were deposited at $\alpha = 85º$, which were subsequently annealed at different temperatures (T_r) and reaction times (t_r) depending on the volume of material to be oxidized. Comprehensive microstructural and compositional characterizations of these oxidized systems were conducted by combining scanning electron microscopy (SEM), Raman spectroscopy (RS), grazing incidence X-ray diffraction (GIXRD) and scanning-transmission electron microscopy (S)TEM techniques, including high-angle annular dark-field imaging (HAADF) and high-resolution (HRTEM) imaging, as well as electron energy-loss spectroscopy (EELS). Once disclosed the role of both reaction parameters and layer thickness on the composition, morphology and structure of the synthesized films, their functional characterization was addressed by means of variable temperature visible-near infrared (vis-NIR) reflectance and resistivity measurements, placing special emphasis on the effect of the different vanadium oxide mixtures on the resulting optical/electrical responses along the metal-to-insulator transition. Additionally, an exhaustive study on the structural (RS at variable temperature), optical and electrical features of the MIT hysteresis of pure VO_2/Si samples was also performed.

2. Materials and Methods

2.1. Deposition process

Films were deposited at room temperature by DC magnetron sputtering from a vanadium metallic target (51 mm diameter and 99.9 atomic % purity) in a homemade deposition chamber. It was evacuated down to 10^{-5} Pa before each run by means of a turbomolecular pump backed by a primary pump. The target was sputtered with a constant current density of $J = 100$ A m^{-2}, leading to a constant target potential of 312 V. Single crystalline (100) n-type (P doped) silicon substrates were placed at a distance of 65 mm from the target center. On the basis of our previous studies[43], porous V films with large surface-to-volume ratios and enhanced reactivity with oxygen were deposited by the GLAD technique. The incidence angle (α) of the incoming particle flux relative to the substrate normal was set at $\alpha = 85^{\circ}$ (the maximum inclination allowed for efficient GLAD deposition, so that the greater the deposition angle, the higher the overall porosity of the film and, therefore, its specific surface area[44]) with no rotation of the substrate (i.e., $\phi = 0$ rev h^{-1}). Argon was injected at a mass flow rate of 2.40 sccm and the pumping speed was maintained at $S = 13.5$ L s^{-1}, leading to a sputtering pressure of 0.3 Pa. Different vanadium nominal thicknesses (100, 200 and 300 nm) were achieved by adjusting the deposition time according to an average deposition rate of 240 nm h^{-1}, which was previously determined for $\alpha = 85^{\circ}$. The real thickness of vanadium films was measured in a Bruker DEKTAK XT 2D contact profilometer.

2.2. Thermal treatments

After deposition, vanadium samples were thermally treated in a homemade reaction system. It consists in an Al_2O_3 tube on a SiC resistors furnace being able to reach temperatures of up to 1500°C, with an attached concentric steel tube with a high-temperature steel covered K-type thermocouple inside. This thermometer bar acts as an axle for a system of horizontal translation. At the end of the metallic tube nearby the furnace, the thermocouple crosses and fixes to a cylinder placed inside this tube, mechanized with a hitch to hang a combustion boat. Thus, the thermometer tip is always placed some millimeters over the center of this boat, which is an alumina crucible, allowing the temperature in the reaction zone to be life-tracked. The other end side also crosses and is fixed to another piece that is part of a handlebar used to slide the specimen holders inside and outside. In this way, by fixing a temperature in the center of the furnace, one is able to control the temperature increase (heating rate) by moving the boat more and more inside the furnace (for a more detailed overview of the reaction system, refer to previous studies[43,45,46]). Consequently, translation routines were prepared for reaching an average heating rate of 42ºC s^{-1}, as well as for adjusting longer or shorter reaction times at a desired temperature. Lastly, all the samples were cooled down in air.

2.3. Structural, compositional and functional characterizations

Topographic scanning electron microscopy (SEM) images were acquired using a FEI Nova NanoSEM microscope operating at 5 kV in order to examine the surface morphology of the films before and after each thermal treatment. Room temperature Raman spectra were recorded on two different systems (HORIBA Scientific LabRAM HR Evolution and Jobin Yvon U1000) using 473 nm and 532 nm laser excitation sources with spectral resolutions of approximately 2 cm^{-1} in the range of 350–900 cm^{-1} (acquisition times of 20 s with an accumulation of 10 spectra) and 100–900 cm^{-1} (acquisition times of 8 s with an accumulation of 2 spectra), respectively. The power of the laser was controlled to avoid the degradation of the sample. Variable temperature Raman measurements were conducted on a confocal Raman micro-spectrometer (Monovista, S-&-I GmbH) equipped with a THMS600 Linkam heating/cooling stage, setting the irradiated laser at 532 nm. The acquisition time was 60 s with an accumulation of two spectra (average spectral resolution of 0.4 cm^{-1} in the range of 80–850 cm^{-1}). GIXRD scans were performed on a Malvern PANalytical Aeris diffractometer (Cu radiation) working at 30 kV (10 mA) and setting a grazing incidence angle of 0.8°. High-resolution transmission electron microscopy (HRTEM) and high-angle annular dark-field imaging (HAADF) studies were carried out in a Thermo Scientific TALOS F200X G2 analytical microscope working at an accelerating voltage of 200 kV. A Gatan Imaging Filter (GIF) Continuum system fitted in the Talos microscope was used for spatially-resolved EELS analysis in scanning (STEM) mode. STEM-EELS 2D spectrum image (SI) data were acquired using a 2.5 mm diameter aperture and 0.05 eV/channel energy dispersion. The convergence and collection semi-angles were set to 10.5 and 20.0 mrad, respectively, and the probe current was about 150 nA. In this configuration, the energy resolution was 0.75 eV. In order to allow accurate chemical shift measurements, the Dual EELS mode was used to record nearly simultaneously both low-loss signal and the V-$L_{2,3}$ and O-K high-loss edges, at each pixel position. Dwell times of about 0.3 seconds per pixel were set to optimize the signal-to-noise ratio. Electron-transparent cross-sectional samples were prepared for TEM observations in a Thermo Scientific Scios 2 DualBeam focused ion beam (FIB) system. The thermochromic optical behavior of the prepared VO_2 films was determined via reflectance spectroscopy using a PerkinElmer Lambda 900 UV/VIS/NIR Spectrometer equipped with a THMS600 Linkam stage for temperature control. Thus, vis-NIR reflectance spectra were recorded at selected temperatures in the wavelength range of 400–3300 nm, using silver as mirror reference. DC electrical resistivity *vs.* temperature measurements of the oxidized films were performed in a custom-made chamber. It is covered in order to have a dark environment, using the four-probe van der Pauw geometry in the temperature range of 25–100ºC with a ramp of 1°C min^{-1} and then back to 25°C with the same negative ramp. Humidity and cleanness were considered as constant. The error associated to all resistivity measurements was always below 1% and the quality of the contacts was checked prior to every run (I/V correlation close to 1) to ensure that an ohmic contact was attained (use of gold coated tips).

3. Results and discussion

3.1. Morphology, structure and composition of the fabricated films

In a first step, pure vanadium GLAD films of 100, 200 and 300 nm nominal thickness were sputtered on silicon substrates at $\alpha = 85^{\circ}$. This deposition configuration and layer thicknesses were selected to promote the subsequent rapid and selective oxidation of the entire coating in air atmosphere, while maximizing VO_2 yields. The real thicknesses of as-deposited V-GLAD films were evidenced by contact profilometry measurements performed in 3 different regions within the same sample. The results obtained are shown in **Table 1**. As can be seen, the real thicknesses move further and further away from the targeted ones as the total thickness of the film increases. This is attributed to the fact that as layer thickness increases in GLAD systems, the deposition process becomes more dominated by events related to the shadowing effect so characteristic of this technique, so that only the larger columns progress to the detriment of the smaller ones[47,48]. This phenomenon also leads to an increase in the overall porosity of the coating. As a result, the surface area in contact with the sputtered particle pathway becomes increasingly limited after exceeding a threshold thickness (deposition process promoted exclusively by the shadowing effects), which can result in a decrease in the overall deposition rate.

Table 1. Nominal (τ_N) and real (τ_R) V-GLAD thicknesses for as-deposited samples together with their annealing conditions. τ_R values were determined by contact profilometry. T_r is the reaction temperature and t_r is the reaction time.

Sample	**τ_N (nm)**	**τ_R (nm)**	**T_r (ºC)**	**t_r (s)**
T100_475_60	100	97 ± 12	475	60
T100_550_1			550	1
T100_550_10				10
T100_550_30				30
T200_475_90	200	160 ± 16	475	90
T200_550_25			550	25
T200_550_45				45
T300_475_120	300	241 ± 21	475	120
T300_550_25			550	25
T300_550_45				45

These fabricated systems were then subjected to different rapid thermal treatments. For this purpose, all the samples were annealed at the same constant heating rate of 42ºC s^{-1} until reaching two reaction temperatures (T_r) close to the limits of the operating window for the synthesis of VO_2 in air: 475 and 550ºC. Such plateau temperatures are maintained for different reaction times (t_r) in order to optimize VO_2 yields as well as to achieve full oxidation of the different layer thicknesses addressed (the greater the V-GLAD volumes, the longer the oxidation times). Thereupon, samples are instantaneously cooled in air (for a detailed outline of the fast thermal treatment procedure, refer to our previous works[43,45,46]). All the annealed samples are listed in **Table 1** together with their treatment conditions and nomenclature.

Figure 1 shows the characteristic SEM topography of the fabricated coatings before and after heat treatment. Consistent with the above assumptions, the surface microstructure of as-deposited samples reveals a higher development of the overall porosity as the

GLAD layer thickness increases, resulting in greater column diameters and surface roughness. On the other hand, oxidized samples generally exhibit a mosaic-like granular structure, which is characteristic of vanadium dioxide on silicon substrates[43]. The formation of different grain sizes is also observed depending on the thermal treatment applied (**Table 2**). As a general rule, it can be noted that longer reaction times lead to a progressive increase in grain size until reaching a maximum of 130–160 nm. The only sample that overcomes this barrier is T100_550_30, exhibiting an about five times larger grain sizes when increasing the reaction time from 10 (51 ± 9 nm) to 30 s (230 ± 72 nm). Likewise, the morphology of these grains is also different in appearance from the other oxidized samples, which leads to think that this event could be related to the emerging formation of other vanadium oxides different from VO_2 (probably with an O/V stoichiometric ratio higher than 2).

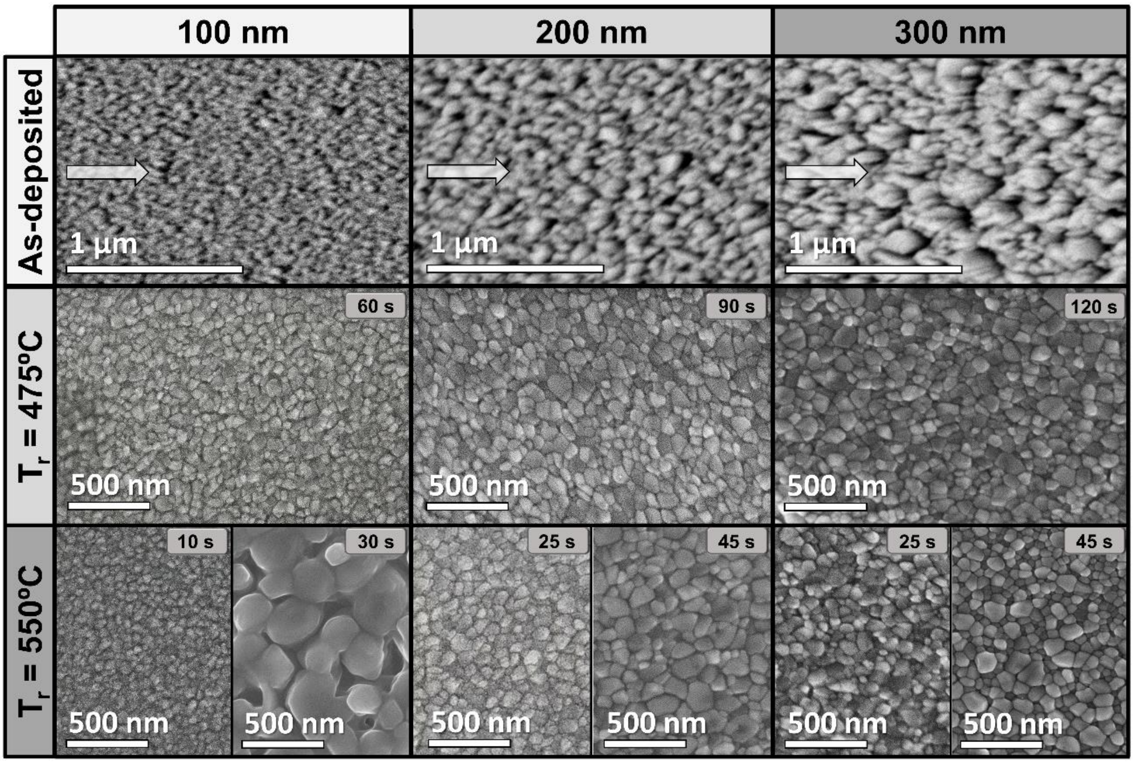

Figure 1. Topographic SEM micrographs of the deposited films before and after annealing. Arrows indicate the direction of the particle flux during each GLAD deposition.

On the other hand, it is also evidenced that, for the same t_r value, higher reaction temperatures result in larger grain sizes. In this regard, it must be noted that thermal treatments at 475ºC require more than twice the reaction time to achieve grain sizes similar to those obtained at 550ºC for the same sample thickness, the latter being another of the parameters that also plays an important role on this issue. Apart from the aforementioned exception, it is worth noting that the grain sizes for samples T100_550_10 and T100_475_60 do not exceed 90 nm. This could be due to the fact that 100 nm V-GLAD samples (note that from this point onwards only nominal layer thicknesses will be referenced in order to simplify and streamline the text) are the least porous, leading to smaller surface-to-volume areas. In other words, such samples are less susceptible to rapid and selective oxidation, hence the limitation of the grain size formed. In any case, it should be remembered that longer reaction times applied on 100 nm thick samples could lead to the undesired formation of other vanadium oxides different from the dioxide (sample T100_550_30).

Table 2. Summary of the average grain sizes for thermally-treated samples. Note that these values were extracted from the analysis of different topographic SEM images.

Sample	**Grain size (nm)**
T100_475_60	69 ± 21
T100_550_10	51 ± 9
T100_550_30	230 ± 72
T200_475_90	112 ± 46
T200_550_25	82 ± 22
T200_550_45	132 ± 31
T300_475_120	120 ± 35
T300_550_25	88 ± 15
T300_550_45	100 ± 28

In order to corroborate the above, room temperature Raman measurements were carried out for all the samples oxidized at 475ºC and 550ºC. The results of these measurements are displayed in **Figure 2(a)** and **(b)**, respectively. These results confirmed the initial assessments so that, according to the Raman spectra reported in the literature for different vanadium oxides[49], there is no doubt that all the samples contain VO_2(M), with the exception of sample T100_550_30, which is composed of VO_2(M) + α-V_2O_5 mixtures. For a better comparison between the two types of recorded signals, **Fig. 2(c)** reveals the Raman spectra of samples T100_550_10 and T100_550_30 for a wider wavenumber range. Nonetheless, these outcomes should be interpreted with great care. This does not necessarily mean that the vast majority of samples consist exclusively of

VO_2(M). Nor does it mean that the entire film is completely oxidized. In this sense, it is worth noting that the Si (substrate) signal appears only for the 100 nm thick samples, being substantially broadened for VO_2(M) + V_2O_5 mixtures (the latter having a greater transparency at visible wavelengths), so it could be the case that the laser is not penetrating through the entire thickness of the film. In addition, there are oxides such as VO, V_2O_3, V_6O_{13}, or even metallic vanadium itself, which either do not give a Raman signal, or it is very weak compared to that of the dioxide[49]. Therefore, further investigations would be needed to better understand the structure and composition of these films.

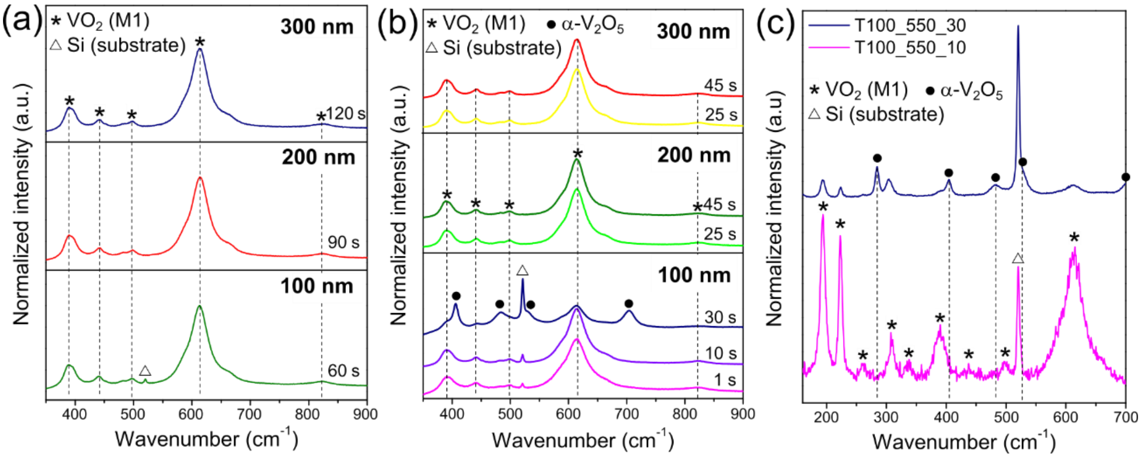

Figure 2. Room temperature Raman spectra for all the samples annealed at (a) 475ºC and (b) 550ºC. (c) Raman spectra recorded for samples T100_550_10 (magenta) and T100_550_30 (blue) at 150–700 cm^{-1}.

Figure 3 shows the GIXRD diffractograms recorded for each of the samples oxidized at 475 and 550ºC. These studies allowed to identify the presence of other oxides such as V_2O_3 (JCPDS Card No. 00-085-1411) and V_6O_{13} (JCPDS Card No. 00-025-1251) forming mixtures with VO_2(M) (JCPDS Card No. 03-065-2358), the latter being always present in all the oxidized samples and thus in fine agreement with what was previously evidenced by RS. In this vein, VO_2 crystallite sizes, calculated from the full width at half maximum (FWHM) of the VO_2 diffraction peaks at about 28° using the Scherrer equation, were determined to be approximately 22–23 nm. It was also confirmed that sample T100_550_30 consists of VO_2(M) + V_2O_5 (JCPDS Card No. 00-041-1426). Likewise, these analyses prove that metallic vanadium becomes fully oxidized even for instantaneous thermal treatments (sample T100_550_1), although giving rise to significant amounts of V_2O_3 (a vanadium oxide with an O/V ratio lower than that of VO_2). Furthermore, it should be highlighted that sample T200_550_45 is the only one formed exclusively by VO_2(M). All the others are formed by VO_2 + V_2O_3 mixtures, which are identified in samples subjected to the lowest t_r for a given reaction temperature; or VO_2(M) + V_6O_{13} mixtures, for increasing layer thicknesses and/or reaction times. Special attention should be paid to sample T100_550_30, whose combination of T_r, t_r and thickness seems to be the only one that overcomes the energy threshold for the activation of reactions leading to the synthesis of V_2O_5. In any case, it should be emphasized that the V-GLAD layer thicknesses as well as the reaction window selected here are suitable for synthesizing VO_2 in air.

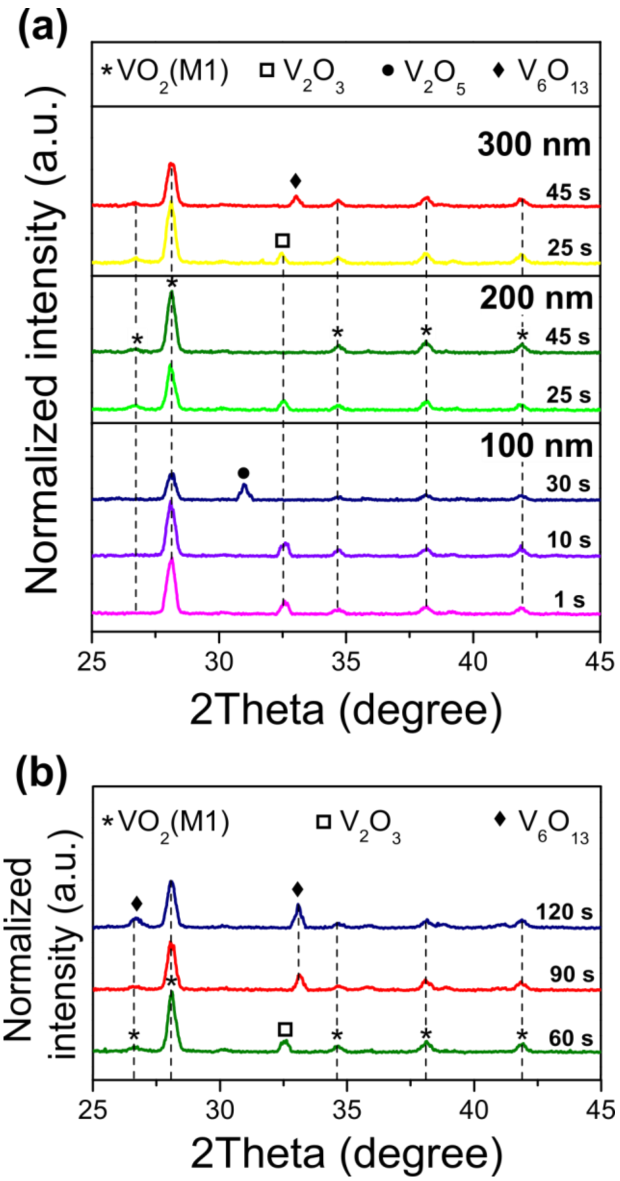

Figure 3. GIXRD diffractograms for V-GLAD samples annealed at (a) 550ºC and (b) 475ºC with reaction times (t_r) ranging from 1 to 120 s.

With the aim of obtaining additional insights into the nanostructure and composition of these synthesized coatings as well as to better understand how oxidation processes take place, analytical (S)TEM studies were performed on samples T100_550_10 and T100_550_30. The results of these explorations are displayed in **Figure 4** and **Figure 5**, respectively. Preliminarily, it can be noticed a considerable increase in the overall thickness of both coatings after thermal treatment (~135 nm for T100_550_10 and ~190 nm for T100_550_30 according to **Fig. 4(a)** and **Fig. 5(a)**, respectively). This is in line with our previous studies[43], which disclosed thicker samples as the coating became more oxygen enriched. In turn, this would also explain why sample T100_550_30, consisting of VO_x mixtures of higher valence states (V^{4+} and V^{5+}), is thicker. Apart from that, **Fig. 4(a)** allows to distinguish two clearly differentiated regions within the T100_550_10 sample: a first relatively dense main layer, denoted as VO_x (I), formed by grains of size similar to those observed by SEM; and a second layer underneath of considerably lower thickness that still preserves, albeit slightly, the tilted column geometry so characteristic of GLAD deposition (VO_x (II)). The latter suggests that this second region could be less oxidized, so that oxidation would occur from the film surface towards the interface with the substrate. **Fig. 4(b–c)** illustrate images corresponding to successive magnifications of a grain located in the region labelled as "VO_x (I)" showing characteristic lattice distances and angles of planes observable along the [120] VO_2(M) zone axis which are identified by the combined study of both HRTEM images and their respective fast Fourier transforms (FFTs), which are spectrums equivalent to the electron diffraction pattern of the area. Furthermore, EELS spectroscopy analyses carried out in different areas of sample T100_550_10 (**Fig. 4(d–e)**) confirm the V^{4+} valence state (VO_2) of this first region, which is characterized by EELS signature signals with higher energy loss of the V-$L_{2,3}$ white lines (L3 position at 516.2 eV), the presence of two peaks in the O-K pre-edge region that correspond to the t_{2g} (around 528.1 eV) and e_g (around 530.7 eV) states, as well as the shoulders visible on the left sides of the L3 and L2 peaks (indicated by arrows)[50,51]. In contrast, the EELS signal recorded in region II (lower energy shift of the V-$L_{2,3}$ lines, a single peak in the O-K pre-edge region) fits more with those reported for the V^{2+}[51,52] and

V^{3+}[50,52] valence states, the latter being consistent with what was previously evidenced by GIXRD. This evidences the presence of V_2O_3 in this sample at regions close to the substrate, and therefore confirms the previous hypothesis that the oxidation process originates from the surface towards the interior of the film.

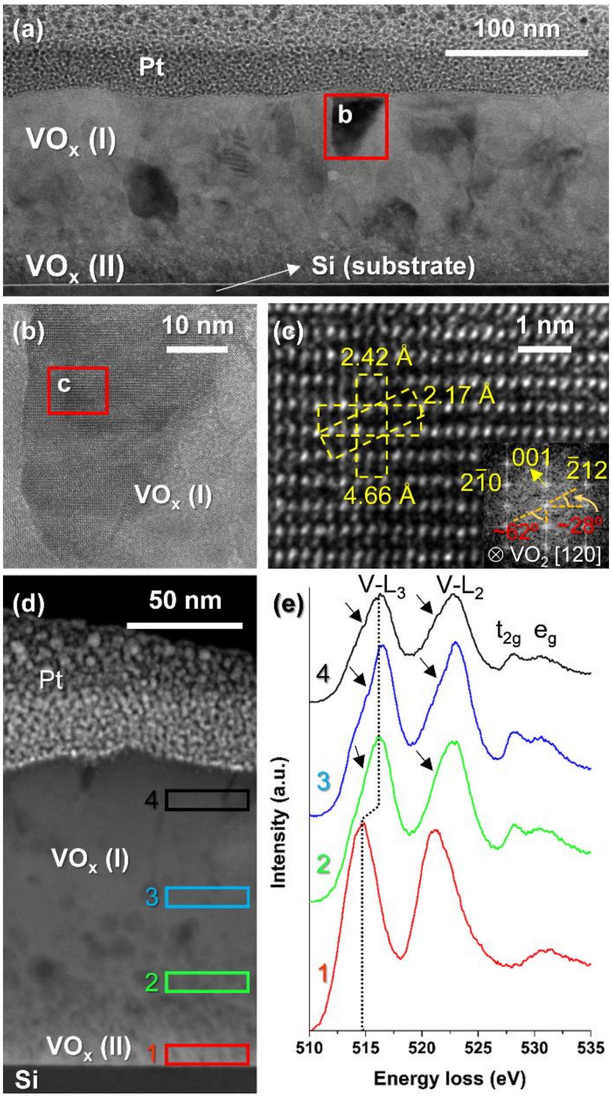

Figure 4. Analytical (S)TEM studies performed on sample T100_550_10. (a) Bright-field (BF) TEM overview of the sample taken with the sample oriented along one of the Si <110> zone axes. (b) High-resolution TEM micrograph depicting a grain belonging to the upper part of the film. (c) HRTEM micrograph of the narrow region highlighted in (b) together with its associated FFT spectrum. (d) High-angle annular dark-field (HAADF) overview of the sample. (e) Integrated EELS spectra corresponding to the areas marked in (d).

On the other hand, sample T100_550_30 shows considerably different characteristics than the previous one. Although two regions can also be distinguished, they are not so obvious in this case, since both their morphology and thickness do not follow an established pattern (see **Fig. 5(a)**). Successive magnifications of a boundary zone between these two regions show interplanar spacings and angles that match with the [124] VO_2(M) orientation (**Fig. 5(b–c)**). However, differently from sample T100_550_10, it appears that, on this occasion, the region denoted as VO_x (II) is the one with the higher valence state oxide. **Fig. 5(d–e)** show the integrated EELS spectra collected in different regions of sample T100_550_30, revealing signature signals corresponding to the valence state V^{4+} (VO_2) and V^{5+} (V_2O_5) for regions furthest (spectra #1–3) and closest (spectrum #4) to the substrate, respectively, according to the trends evidenced in the literature. All things considered, it becomes evident that the VO_2(M) + V_2O_5 system evolves in a totally different way from the previous one, giving rise to more irregular and inhomogeneous coatings with grain sizes comparable to the total film thickness. This latter could somehow explain the presence of vanadium pentoxide close to the interface with the silicon substrate. In any case, it should not be forgotten that this sample is the only one that moves away from the trends observed for the rest of the annealed samples in terms of composition and surface microstructure.

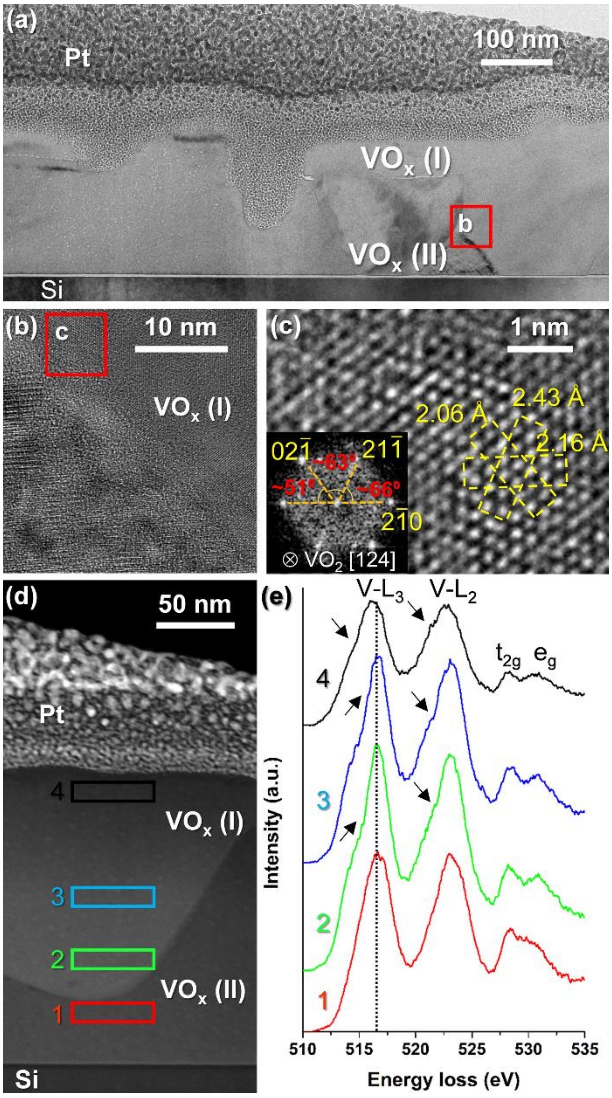

Figure 5. Analytical (S)TEM studies performed on sample T100_550_30. (a) Bright-field (BF) TEM overview of the sample along one of the Si <110> zone axes. (b) High-resolution TEM detail of grain boundary zone. (c) HRTEM micrograph of the narrow region highlighted in (b) together with its associated FFT spectrum. (d) High-angle annular dark-field (HAADF) overview of the sample. (e) Integrated EELS spectra corresponding to the areas marked in (d).

In order to explore the features of the structural phase transition (SPT) of the pure VO_2/Si coating (sample T200_550_45, according to GIXRD studies), further Raman spectroscopy analyses were carried out at different temperatures between 25°C and 100°C for consecutive heating/cooling cycles (**Figure 6**). In this sense, **Fig. 6(a)** shows the progressive disappearance of the Raman bands associated with the monoclinic VO_2 phase once T_c is exceeded during heating cycles, to give way to the rutile VO_2(R) phase, which is characterized by the absence of Raman signal (metallic behavior)[53]. The contrary trend is observed in **Fig. 6(b)**, with a $VO_2(R) \rightarrow VO_2(M)$ phase change at lower critical temperatures during cooling. **Fig. 6(c)** displays the MIT hysteresis resulting from the variation of the normalized Raman signal of the VO_2(M) band at ~194 cm^{-1} for consecutive heating/cooling cycles, highlighting a clear thermochromic response of the synthesized VO_2/Si coating associated with the reversible monoclinic to rutile phase change. T_c values, estimated from the derivatives curves of the Raman intensity *vs.* temperature plots with a Gaussian fit, show slightly higher temperatures than the conventional value reported for pure VO_2 films during the heating cycle (~68°C). However, this shifting toward higher temperatures was also observed in our previous work[43]. In addition, these experiments also revealed a hysteresis loop width (W_H, given by $T_{c(heating)} - T_{c(cooling)}$) of about 15ºC. In any case, it is worth mentioning that these parameters will be reassessed/compared once the optical and electrical characterization of the synthesized VO_2-based films, including sample T200_550_45, has been addressed.

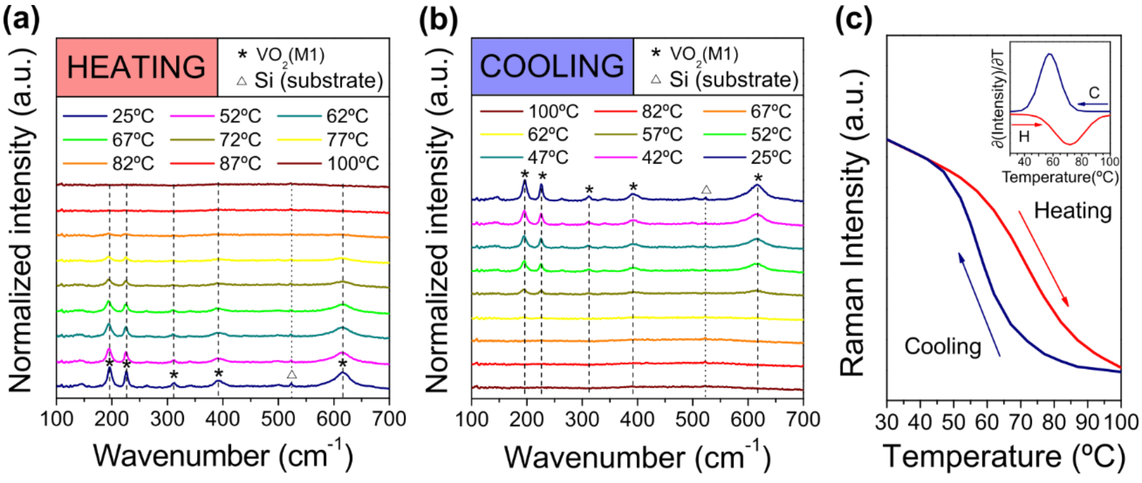

Figure 6. Raman spectra recorded for sample T200_550_45 at multiple temperatures between 25 and 100ºC during consecutive (a) heating and (b) cooling cycles. (c) Thermal evolution of the intensity of the VO_2(M) Raman band at 194 cm^{-1} during heating (red) and cooling (blue) cycles. The inset shows the derivative of each kinetic thermochromic cycle (the derivative of the cooling is plotted in absolute values).

3.2. Functional metal-to-insulator responses

3.2.1. Vis-NIR reflectance at variable temperature

In the first instance, vis-NIR reflectance measurements (400–3300 nm) were conducted at 25ºC and 110ºC on samples annealed at 550ºC, covering each of the four possible scenarios: (i) VO_2 + V_2O_3 mixtures (sample T100_550_10); (ii) VO_2 + V_2O_5 mixtures (sample T100_550_30); (iii) pure VO_2 (sample T200_550_45); and (iv) VO_2 + V_6O_{13} mixtures (sample T300_550_45). These spectra are shown in **Figure 7(a–b)**. Additionally, **Fig. 7(c–d)** represents the rate of change in reflectance experienced by each of these samples defined by the $\Delta R/R_0$ ratio, where R_0 are the reflectance values at 25ºC for the wavelength range previously established. The information extracted from all these measurements is summarized in **Table 3**, which lists the maximum change in reflectance (ΔR_{max}), the wavelength at which this occurs (λ_{max}), as well as the limiting wavelength beyond which ΔR only takes positive values (λ_0).

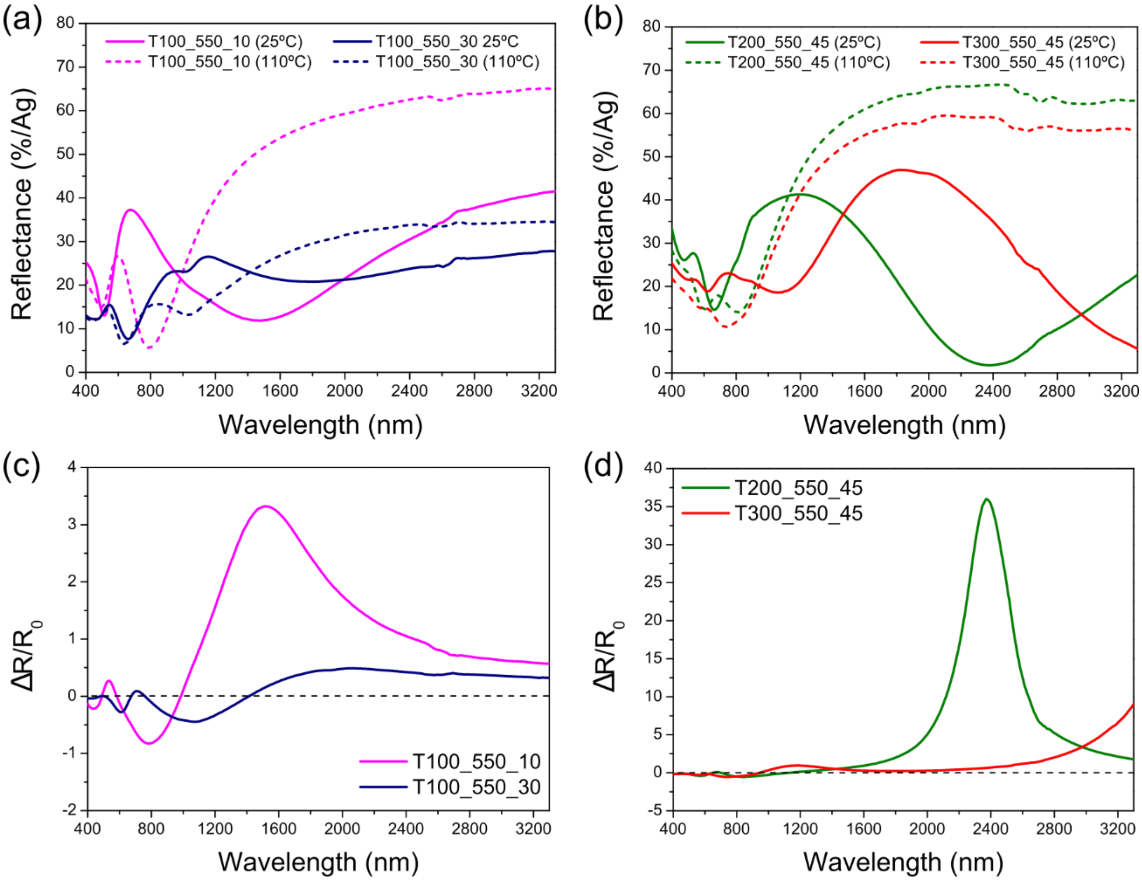

Figure 7. Reflectance spectra recorded at 25ºC (solid lines) and 110ºC (dashed lines) for samples (a) T100_550_10 & T100_550_30 and (b) T200_550_45 & T300_550_45. Rate of change in reflectance $(R - R_0)/R_0$ at 25ºC (R_0) and 110ºC (R) for samples (c) T100_550_10 & T100_550_30 and (d) T200_550_45 & T300_550_45.

As generally discerned in **Fig. 7**, the resulting optical responses for each of the examined samples are very diverse. On the one hand, sample T100_550_10 shows a maximum change in reflectance (ΔR_{max} = 39.9%) at 1515 nm, which is quite significant.

By contrast, sample T100_550_30 presents substantially smaller reflectance variations over the whole wavelength range explored, reaching its maximum (ΔR_{max} = 10.5%) at further wavelengths (λ_{max} = 2060 nm). On another note, while the sample consisting exclusively of vanadium dioxide (i.e. T200_550_45) exhibits reflectance changes of more than 30% above 1600 nm (ΔR_{max} = 64.8% at 2375 nm), it is thought that the maximum ΔR for sample T300_550_45 would be rather centered within the mid-wavelength infrared (MWIR) spectral band (note that a maximum reflectance variation of 50.0% was registered at 3300 nm, which is the limiting wavelength for the spectral window considered). In any case, although, unlike what was observed for sample T100_550_30, most of the coatings show similar metallic responses at 110ºC, it should be stressed that sample T200_550_45 exhibits a higher NIR reflectance than the rest despite being thinner than T300_550_45, which could be attributed to the fact that it only consists of VO_2. Likewise, the main difference between the optical responses of the latter two samples lies in their spectra at room temperature, which are relatively comparable in terms of their signature signals, but with a shift towards longer wavelengths in the case of T300_550_45.

Table 3. Main features of the reflectance changes experienced by different annealed samples in the vis-NIR range when increasing temperature. ΔR_{max} indicates the maximum value taken by ΔR (which is given by the difference between the reflectance values at 110ºC and 25ºC, respectively); λ_{max} is the wavelength at which ΔR_{max} occurs; and λ_0 denotes the limiting wavelength beyond which ΔR only takes positive values.

Sample	**ΔR_{max} (%)**	**λ_{max} (nm)**	**λ_0 (nm)**
T100_550_10	39.9	1515	990
T100_550_30	10.5	2060	1415
T200_550_45	64.8	2375	1130
T300_550_45	50.0	3300	945

Taking as a model the optical response associated with the VO_2/Si coating (i.e. sample T200_550_45), it is possible to observe how the VO_x mixtures previously identified exhibit optical responses that, in one way or another, deviate from this ideality. For this purpose, special attention will be paid to the values taken by the parameters listed in **Table 3**. In this regard, the values of λ_{max} mark the onset of free-carrier dominated reflectance (free-carrier absorption typical of semiconductor systems) for measurements at 25°C, while λ_0 determines the wavelength from which effective reflectance modulation is achieved. On the one hand, sample T100_550_10 (VO_2 + V_2O_3) is the one that exhibits ΔR_{max} at the lowest wavelength, resulting in reflectance modulations of about 20–40% between 1200–3300 nm. On the contrary, sample T100_550_30, formed by VO_2 + V_2O_5, is the one that shows the weakest metallic response ($R < 35\%$ in the NIR) at 110ºC. This phenomenon, which can be directly attributed to the presence of pentoxide or to the formation of reduced amounts of dioxide, translates into a considerable detriment of the thermochromic properties of the coating.

Conversely, sample T300_550_45 (VO_2 + V_6O_{13} mixes) presents values of λ_0 and λ_{max} lower and higher, respectively, than those of sample T200_550_45. This somehow implies a larger application window, although at the cost of a decrease (although not as severe as that recorded for sample T100_550_30) of the NIR reflectance for the VO_2(R) metallic phase. Similarly, this sample shows $\Delta R > 30\%$ at wavelengths above 2500 nm, although at the expense of discrete changes in reflectance (10–20%) between 1000–2000 nm. In any case, it should be highlighted that the changes in NIR reflectance accomplished in this study, especially those of sample T200_550_45, are outstanding compared to the best values reported so far in the literature for similar VO_2 coatings[54–58]. Hence, it seems clear that both VO_2 + V_2O_3 or VO_2 + V_6O_{13} mixtures could be advantageous for optical applications within specific infrared windows such as SWIR and MWIR, respectively. Also noteworthy is the fact that similar trends and optical responses were observed for the equivalent VO_x mixtures achieved at 475°C (for more information, refer to Supplementary Material, Section I), again demonstrating the suitability of the selected thermal treatment window in terms of temperature and reaction times.

Figure 8 shows the reflectance changes experienced by the best 100, 200 and 300 nm thick samples achieved at 550ºC during consecutive heating/cooling cycles at temperatures between 25–110ºC. Note that this outline allows a better appreciation of the progressive shifting of absorption edge toward larger wavelengths for the semiconducting behavior linked to VO_2(M) as both the film thickness and the overall O/V stoichiometric ratio of the film increase. Notwithstanding, according to the literature, this phenomenon is rather due to the Burstein-Moss effect, which becomes more significant with decreasing the grain size as well as the appearance of impurities and defects[59,60]. Likewise, it can be observed the great reflectance variations that these samples experience in the 400–3300 nm range at temperatures below and above T_c during heating and cooling cycles. Therefore, it seems clear that, for a better determination of the hysteresis loops, the thermal evolution of the reflectance for these samples should be performed at a fixed wavelength from λ_{max} onwards.

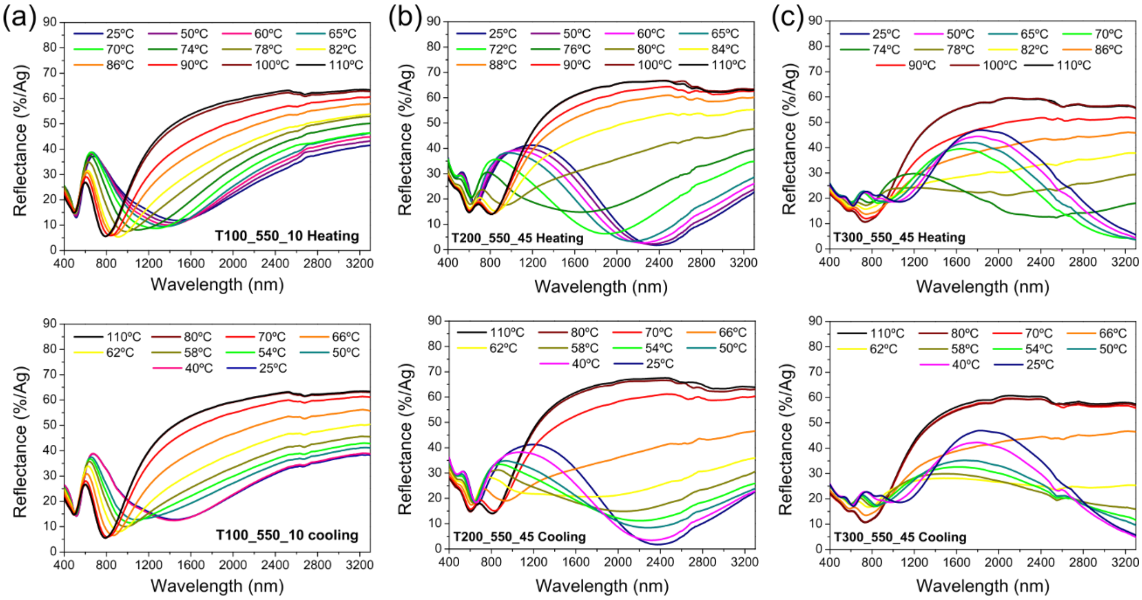

Figure 8. Vis-NIR reflectance spectra of samples (a) T100_550_10, (b) T200_550_45 and (c) T300_550_45, recorded gradually increasing (top) or decreasing (bottom) the temperature.

Figure 9 displays the kinetic evolution of the reflectance at λ_{max} for samples T100_550_10 (**Fig. 9(a)**), T200_550_45 (**Fig. 9(b)**) and T300_550_45 (**Fig. 9(c)**) during consecutive heating and cooling cycles. **Table 4** lists the transition temperatures, at heating ($T_{c(heating)}$) and cooling ($T_{c(cooling)}$), calculated from the derivatives of the sigmoidal fits (Boltzmann function) of the reflectance *vs.* temperature curves, considering the peaks as the temperature of the minimum variation rate (insets in **Fig. 9**), together with the width of the hysteresis loop (W_H). In the first instance, it can be seen that moving away from the ideality of the VO_2/Si system leads to increases (which are more substantial for the specific case of VO_2 + V_2O_3 mixtures) of $T_{c(heating)}$ above the 78ºC recorded for the sample T200_550_45, which is already high in itself. In contrast, $T_{c(cooling)}$ values for this group of samples are almost similar (63–64°C), resulting in greater hysteresis widths for mixtures of vanadium oxides. Generally, the increase in W_H has been related to the presence of dopants, defects or impurities[61,62], as well as the existence of additional energy barriers due to the residual stress associated with the rapid annealing treatments addressed here, which can delay the phase transition upon heating or cooling[63]. Nevertheless, it should be noted that the hysteresis width for all these samples are consistent with those reported for VO_2 polycrystalline films (W_H > 10ºC)[64].

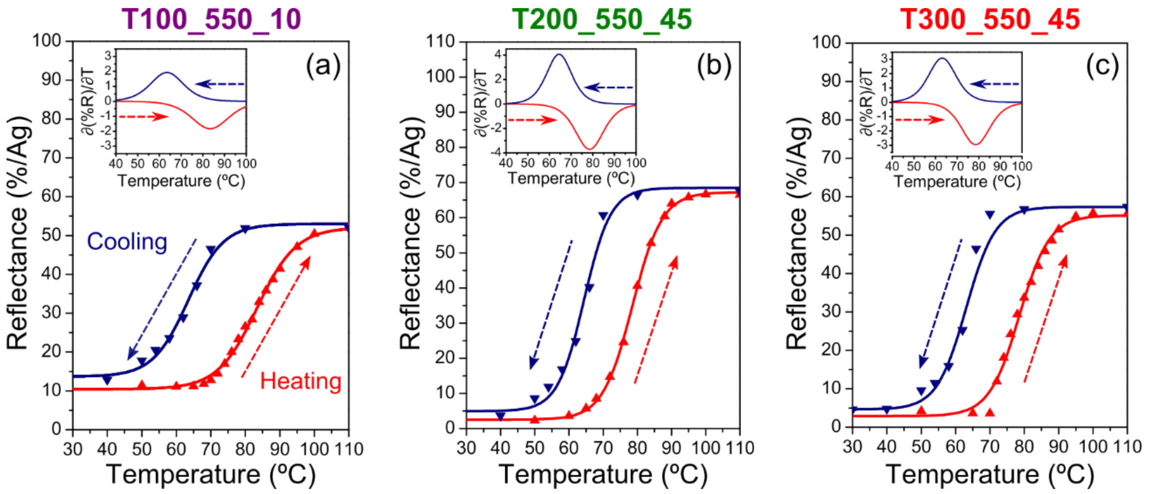

Figure 9. Thermal evolution of the optical reflectance of samples (a) T100_550_10, (b) T200_550_45 and (c) T300_550_45 evaluated at their λ_{max} during heating (red symbols) and cooling (blue symbols) cycles. Solid lines denote the sigmoidal fits (Boltzmann function) of the experimental results for each single kinetic cycle. The insets show the derivatives of such fits (the derivatives of the heating cycles are plotted in absolute values).

Before concluding this section, it is worth highlighting once again the remarkable optical performances of samples T200_550_45 and T300_550_45, which not only exhibit changes in reflectance above 50% adapted for different wavelength ranges within the NIR window, but also reflectance values close to 0% at room temperature (see **Fig. 9 (b–c)**). This makes such systems of potential interest for multiple optical applications (switches, filters, modulators, etc.).

Table 4. Main features of the thermochromic hysteresis loops illustrated in **Fig. 9**. T_c(heating) denotes the temperatures of the MIT on heating; T_c(cooling) indicates the temperatures of the MIT on cooling; and W_H is the hysteresis loop width given by T_c(heating) – T_c(cooling).

Sample	**T_c (heating) (ºC)**	**T_c (cooling) (ºC)**	**W_H (ºC)**
T100_550_10	83	63	20
T200_550_45	78	64	14
T300_550_45	79	63	16

3.2.2. DC Electrical Resistivity *vs.* temperature

The comprehensive characterization of the fabricated coatings is culminated by performing resistivity *vs.* temperature measurements to assess the features of their semiconductor-to-metal electrical transitions. In this sense, it should be mentioned that certain difficulties were encountered when carrying out such measurements given the substrate type (Si doped with P) as well as the electrical characteristics of some of the oxides formed in the VO_x mixtures (note that V_2O_3 exhibits room temperature electrical conductivities almost six orders of magnitude higher than those of VO_2[65]). This is why the 100 nm samples could not be measured. On the other hand, V_6O_{13} also presents a conductivity at 25ºC three orders of magnitude higher than that of VO_2[66]. That is why, although the MIT hysteresis can be recorded for VO_2 + V_6O_{13} mixtures, the orders of magnitude of such drops in resistivity are practically negligible (for more details on the results obtained for these samples, refer to the Supplementary Material, section II). Thus, these findings were considered as not representative of the thermochromic performance associated with such coatings. Better results were obtained for the T200_550_45 sample (formed exclusively by VO_2) as can be seen in **Figure 10**.

However, given the above reasons, the registered resistivity drop was once more rather discrete (only ~0.7 compared to 3–4 orders of magnitude expected for the resistivity drop in VO_2 films according to the literature[67–69]). In any case, such measurements allowed the evaluation of the electrical MIT hysteresis of this sample.

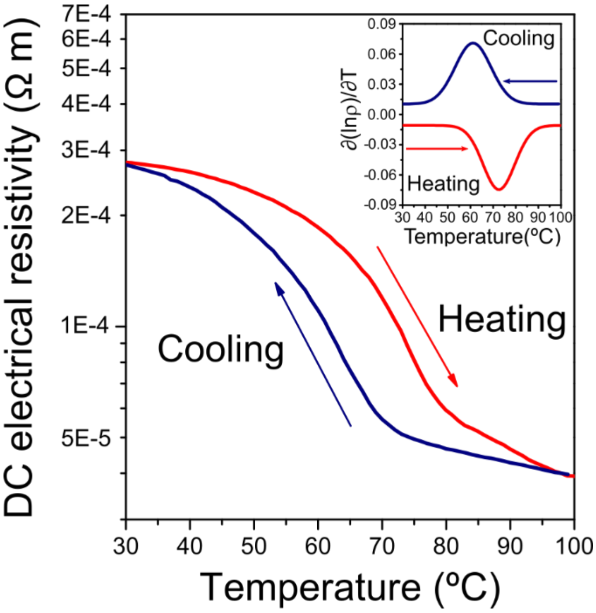

Figure 10. Changes in electrical resistivity with temperature registered for sample T200_550_45 during heating (red) and cooling (blue) cycles. The inset shows the Gaussian fit for the derivative of each kinetic thermochromic cycle (the derivative of the cooling cycle is plotted in absolute values).

3.3. Discussion on the structure-properties MIT variances for the VO_2/Si system

At this point, the distinctive features of the different MIT hysteresis (structural, optical, electrical) recorded for the same VO_2/Si sample will be compared. **Table 5** shows a comparison of the characteristic parameters that evaluate the hysteresis loops of sample

T200_550_45 extracted by RS, spectral reflectance and resistivity measurements, all of them at variable temperature. In this sense, the noticeable difference between the features of each of these hysteresis has been commonly associated with the different nature of the optical and structural MIT[70]. Likewise, it has also been reported that the electrical properties in VO_2 systems can be understood by analyzing the properties of the SPT[71,72]. This explains why the structural and electrical characterizations of this sample evidence more similar results in terms of T_c and W_H values. In addition, the values of these parameters resulting from the resistivity *vs.* temperature measurements are comparable to those reported in the literature[70]. That is not the case for the T_c values obtained by reflectance measurements, which are abnormally high (even in contrast to what was evidenced in our most recent studies dealing with the fabrication of VO_2-based coatings on glass substrates[73,74]). This feature has generally been attributed to deposition conditions and post-processing[75], so that the size of the synthesized grains as well as their homogeneity could affect this phenomenon. Likewise, residual strain along the c-axis[76] and oxygen adsorption[77] can also promote this increase in MIT temperature. In any case, it was previously observed that structural and/or compositional heterogeneity leads to higher $T_{c(heating)}$ (see **Table 4**).

Table 5. Summary of the structural, optical and electrical features of the MIT hysteresis for sample T200_550_45.

Technique	**T_c (heating) (ºC)**	**T_c (cooling) (ºC)**	**W_H (ºC)**
Raman spectroscopy	72	57	15
Vis-NIR reflectance	78	64	14
DC electrical resistivity	73	61	12

In the light of the foregoing, it has been demonstrated that the rapid and controlled oxidation in air of V-GLAD films deposited on silicon substrates gives rise to VO_2-based coatings at temperatures between 475–550ºC and reaction times below 120 s. Thanks to the modulation of the layer thickness and the heat treatment parameters, it was possible to synthesize thermochromic coatings of different compositions exhibiting very good optical performances (ΔR = 30–65%) adapted to specific wavelengths within the NIR window. This fact makes the synthesized systems of great interest for applications in optical switches or filters. Likewise, the synthesis of pure VO_2 films on silicon was also attained. On the basis of the great SPT evidenced by Raman spectroscopy (structural and electrical responses are closely linked), it is thought that the order of magnitude of resistivity drop resulting from the VO_2/Si system could be significantly improved by using undoped silicon. Under this circumstance, the synthesized systems would also be applicable in a multitude of optoelectronic and electronic smart devices. It is therefore concluded that the strategies described throughout this work open up a more environmentally friendly (thermal annealing in the absence of reactive gases, liquid solutions or catalysts without special pressure requirements) and economically viable (low thermal budget associated with moderate temperatures and relatively short oxidation times) pathway for the fabrication of high-performance VO_2-based films on silicon platforms.

4. Conclusions

An advantageous strategy for the fabrication of high-performance VO_2-based thermochromic films on silicon for application in smart devices has been reported. This procedure involves the GLAD deposition of metallic vanadium films with thicknesses between 100 and 300 nm and their subsequent fast oxidations in air atmosphere at 475–

550ºC for reaction times between 1–120 s. By modulating the V-GLAD layer width and the thermal treatment parameters, high VO_2(M) yields were achieved. Comprehensive characterizations of the structure and composition of the fabricated coatings by SEM and TEM electron microscopies, Raman spectroscopy, and X-ray diffraction showed that all samples were, in most cases, composed of mixtures of VO_2(M) and other vanadium oxides such as V_2O_3, V_6O_{13} or V_2O_5. A 200 nm thick pure VO_2/Si film was also synthesized at 550°C for 45 s. On the other hand, structural, optical and electrical analyses carried out at different temperatures between 25–110ºC allowed to evaluate the thermochromic performance of such coatings. In this sense, vis-NIR reflectance measurements evidenced changes in reflectance between insulator-metallic states sometimes higher than those reported so far for similar VO_2/Si systems (note that several samples exhibited ΔR = 30–65% in the NIR range) with a remarkable maximum variation of 64.8% reached for the pure VO_2 film at a wavelength of 2375 nm. By controlling the structure and composition of the coatings, effective tuning of the wavelength window at which the ΔR_{max} peaks in $VO_2 + V_2O_3$ or V_6O_{13} mixtures could also be achieved. The MIT hysteresis loops recorded by the optical characterization of these samples revealed $T_{c(heating)}$ values up to 15ºC above the expected value for pure VO_2 (~68ºC), becoming higher for mixtures of vanadium oxides. This phenomenon was associated to several causes such as deposition and annealing processes, the presence of residual stress, defects, dopants, etc. Conversely, although the electrical characterization of most of VO_2-based systems fabricated was hindered by several factors (use of doped silicon, formation of other high conductivity vanadium oxides), the electrical MIT hysteresis for the VO_2/Si system was unraveled, emphasizing lower T_c than those associated with the optical MIT, but similar to those registered through variable temperature Raman spectroscopy (structural MIT). These promising results not only demonstrate the feasibility of the alternative methodologies addressed, but also the appeal of the manufactured systems for their integration into a multitude of optical, optoelectronic and/or electronic smart devices.

Acknowledgements

A. J. Santos would like to thank the University of Cádiz and the Spanish Ministerio de Universidades for the concession of a “Margarita Salas” postdoctoral fellowship funded by the European Union - NextGenerationEU (2021-067#9663/PN/MS-RECUAL/CD). University of Cádiz and IMEYMAT are also acknowledged by financing the mutual facilities available at the UCA R&D Central Services (SC-ICYT), the UCA project references “PUENTE PR2020-003 and PR2022-027” and “OTRI AT2019/032”, and the IMEYMAT project reference “LÍNEAS PRIORITARIAS PLP2021120-1”. This work was supported by the Spanish State R&D project (Retos y Generación de Conocimiento) ref. PID2020–114418RBI00. The regional government of Andalusia with FEDER co-funding also participates through the projects AT-5983 Trewa 1157178 and FEDER-UCA18-10788. J. J. Jiménez and F. M. Morales acknowledge “Fondo Social Europeo y la Consejería de Transformación Económica, Industria, Conocimiento y Universidades” of this same institution (2021-001/PAI/PAIDI2020/CD). This work was partly supported by the French RENATECH network, FEMTO-ST technological facility, by the Region Bourgogne-Franche-Comté and by EIPHI Graduate School (Contract “ANR–17–EURE–0002”).

Data availability statement

Data will be made available on request.

Declaration of Competing Interest

The authors declare that they have no known competing financial interests or personal relationships that could have appeared to influence the work reported in this paper.

REFERENCES

[1] F.J. Morin, Oxides which show a metal-to-insulator transition at the neel temperature, Phys. Rev. Lett. 3 (1959) 34–36. doi:10.1103/PhysRevLett.3.34.

[2] T.C. Chang, X. Cao, S.H. Bao, S.D. Ji, H.J. Luo, P. Jin, Review on thermochromic vanadium dioxide based smart coatings: from lab to commercial application, Adv. Manuf. 6 (2018) 1–19. doi:10.1007/s40436-017-0209-2.

[3] K. Khaled, U. Berardi, Current and future coating technologies for architectural glazing applications, Energy Build. 244 (2021) 111022. doi:10.1016/j.enbuild.2021.111022.

[4] A.J. Santos, N. Martin, J. Outón, A. Casas-Acuña, E. Blanco, R. García, F.M. Morales, Atmospheric flash annealing of low-dimensional vanadium nanolayers sputtered on glass substrates, Surf. Interfaces. 34 (2022) 102313. doi:10.1016/j.surfin.2022.102313.

[5] G. Savorianakis, K. Mita, T. Shimizu, S. Konstantinidis, M. Voué, B. Maes, VO_2 nanostripe-based thin film with optimized color and solar characteristics for smart windows, J. Appl. Phys. 129 (2021) 185306. doi:10.1063/5.0049284.

[6] Y. Cui, Y. Ke, C. Liu, Z. Chen, N. Wang, L. Zhang, Y. Zhou, S. Wang, Y. Gao, Y. Long, Thermochromic VO_2 for energy-efficient smart windows, Joule. 2 (2018) 1707–1746. doi:10.1016/j.joule.2018.06.018.

[7] N. Shen, S. Chen, R. Huang, J. Huang, J. Li, R. Shi, S. Niu, A. Amini, C. Cheng, Vanadium dioxide for thermochromic smart windows in ambient conditions, Mater. Today Energy. 21 (2021) 100827. doi:10.1016/j.mtener.2021.100827.

[8] M. Maaza, D. Hamidi, A. Simo, T. Kerdja, A.K. Chaudhary, J.B. Kana Kana, Optical limiting in pulsed laser deposited VO_2 nanostructures, Opt. Commun. 285 (2012) 1190–1193. doi:10.1016/j.optcom.2011.09.057.

[9] J. Parra, J. Navarro-Arenas, M. Menghini, M. Recaman, J. Pierre-Locquet, P. Sanchis, Low-threshold power and tunable integrated optical limiter based on an ultracompact VO_2/Si waveguide, APL Photonics. 6 (2021) 121301. doi:10.1063/5.0071395.

[10] S. Cueff, J. John, Z. Zhang, J. Parra, J. Sun, R. Orobtchouk, S. Ramanathan, P. Sanchis, VO_2 nanophotonics, APL Photonics. 5 (2020) 110901. doi:10.1063/5.0028093.

[11] K.J. Miller, R.F. Haglund, S.M. Weiss, Optical phase change materials in integrated silicon photonic devices: review, Opt. Mater. Express. 8 (2018) 2415–2429. doi:10.1364/ome.8.002415.

[12] J. Parra, T. Ivanova, M. Menghini, P. Homm, J.P. Locquet, P. Sanchis, All-optical hybrid VO_2/Si waveguide absorption switch at telecommunication wavelengths, J. Light. Technol. 39 (2021) 2888–2894. doi:10.1109/JLT.2021.3054942.

[13] K.A. Hallman, K.J. Miller, A. Baydin, S.M. Weiss, R.F. Haglund, Sub-picosecond response time of a hybrid VO_2:silicon waveguide at 1550 nm, Adv. Opt. Mater. 9 (2021) 2001721. doi:10.1002/adom.202001721.

[14] A.M. Selman, M.J. Kadhim, Fabrication of high sensitivity and fast response IR photodetector based on VO_2 nanocrystalline thin films prepared on the silicon substrate, Opt. Mater. (Amst). 131 (2022) 112664.

doi:10.1016/j.optmat.2022.112664.

[15] Z.A. Umar, R. Ahmed, H. Asghar, U. Liaqat, A. Fayyaz, M.A. Baig, VO_2 thin film based highly responsive and fast VIS/IR photodetector, Mater. Chem. Phys. 290 (2022) 126655. doi:10.1016/j.matchemphys.2022.126655.

[16] X. Chen, J. Dai, Optical switch with low-phase transition temperature based on thin nanocrystalline VO_x film, Optik. 121 (2010) 1529–1533. doi:10.1016/j.ijleo.2009.02.016.

[17] J. Qi, D. Zhang, Q. He, L. Zeng, Y. Liu, Z. Wang, A. Zhong, X. Cai, F. Ye, P. Fan, Independent regulation of electrical properties of VO_2 for low threshold voltage electro-optic switch applications, Sensors Actuators A Phys. 335 (2022) 113394. doi:10.1016/j.sna.2022.113394.

[18] A. Rana, C. Li, G. Koster, H. Hilgenkamp, Resistive switching studies in VO_2 thin films, Sci. Rep. 10 (2020) 3293. doi:10.1038/s41598-020-60373-z.

[19] A. Annadi, M. Bohra, V. Singh, Modulations in electrical properties of sputter deposited vanadium oxide thin films: Implication for electronic device applications, Thin Solid Films. 758 (2022) 139451. doi:10.1016/j.tsf.2022.139451.

[20] O. Murtagh, B. Walls, I. V. Shvets, Controlling the resistive switching hysteresis in VO_2 thin films via application of pulsed voltage, Appl. Phys. Lett. 117 (2020) 063501. doi:10.1063/5.0017784.

[21] Z. Yang, C. Ko, S. Ramanathan, Oxide electronics utilizing ultrafast metal-insulator transitions, Annu. Rev. Mater. Res. 41 (2011) 337–367.

doi:10.1146/annurev-matsci-062910-100347.

[22] M. Benkahoul, M. Chaker, J. Margot, E. Haddad, R. Kruzelecky, B. Wong, W. Jamroz, P. Poinas, Thermochromic VO_2 film deposited on Al with tunable thermal emissivity for space applications, Sol. Energy Mater. Sol. Cells. 95 (2011) 3504–3508. doi:10.1016/j.solmat.2011.08.014.

[23] M.G. Krishna, Y. Debauge, A.K. Bhattacharya, X-ray photoelectron spectroscopy and spectral transmittance study of stoichiometry in sputtered vanadium oxide films, Thin Solid Films. 312 (1998) 116–122. doi:10.1016/s0040-6090(97)00717-7.

[24] A. Perucchi, L. Baldassarre, P. Postorino, S. Lupi, Optical properties across the insulator to metal transitions in vanadium oxide compounds, J. Phys. Condens. Matter. 21 (2009) 323202. doi:10.1088/0953-8984/21/32/323202.

[25] E. Hryha, E. Rutqvist, L. Nyborg, Stoichiometric vanadium oxides studied by XPS, Surf. Interface Anal. 44 (2012) 1022–1025. doi:10.1002/sia.3844.

[26] Y.-B. Kang, Critical evaluation and thermodynamic optimization of the VO–$VO_{2.5}$ system, J. Eur. Ceram. Soc. 32 (2012) 3187–3198. doi:10.1007/s11663-020-01939-0.

[27] G. Xu, P. Jin, M. Tazawa, K. Yoshimura, Thickness dependence of optical properties of VO_2 thin films epitaxially grown on sapphire (0001), Appl. Surf. Sci. 244 (2005) 449–452. doi:10.1016/j.apsusc.2004.09.157.

[28] J. Bian, M. Wang, H. Sun, H. Liu, X. Li, Y. Luo, Y. Zhang, Thickness-modulated metal–insulator transition of VO_2 film grown on sapphire substrate by

MBE, J. Mater. Sci. 51 (2016) 6149–6155. doi:10.1007/s10853-016-9863-1.

[29] Y. Cui, S. Ramanathan, Substrate effects on metal-insulator transition characteristics of rf-sputtered epitaxial VO_2 thin films , J. Vac. Sci. Technol. A Vacuum, Surfaces, Film. 29 (2011) 041502. doi:10.1116/1.3584817.

[30] M. Taha, S. Walia, T. Ahmed, D. Headland, W. Withayachumnankul, S. Sriram, M. Bhaskaran, Insulator-metal transition in substrate-independent VO_2 thin film for phase-change devices, Sci. Rep. 7 (2017) 17899. doi:10.1038/s41598-017-17937-3.

[31] J. Narayan, V.M. Bhosle, Phase transition and critical issues in structure-property correlations of vanadium oxide, J. Appl. Phys. 100 (2006) 103524. doi:10.1063/1.2384798.

[32] L. Kang, Y. Gao, Z. Zhang, J. Du, C. Cao, Z. Chen, H. Luo, Effects of annealing parameters on optical properties of thermochromic VO_2 films prepared in aqueous solution, J. Phys. Chem. C. 114 (2010) 1901–1911. doi:10.1021/jp909009w.

[33] J. Jeong, Z. Yong, A. Joushaghani, A. Tsukernik, S. Paradis, D. Alain, J.K.S. Poon, Current induced polycrystalline-to-crystalline transformation in vanadium dioxide nanowires, Sci. Rep. 6 (2016) 37296. doi:10.1038/srep37296.

[34] J. Duchene, M. Terraillon, M. Pailly, R.F. and D.C. reactive sputtering for crystalline and amorphous VO_2 thin film deposition, Thin Solid Films. 12 (1972) 231–234. doi:10.1016/0040-6090(72)90081-8.

[35] R. Binions, G. Hyett, C. Piccirillo, I.P. Parkin, Doped and un-doped vanadium

dioxide thin films prepared by atmospheric pressure chemical vapour deposition from vanadyl acetylacetonate and tungsten hexachloride: The effects of thickness and crystallographic orientation on thermochromic properties, J. Mater. Chem. 17 (2007) 4652–4660. doi:10.1039/b708856f.

[36] Y.L. Wang, X.K. Chen, M.C. Li, R. Wang, G. Wu, J.P. Yang, W.H. Han, S.Z. Cao, L.C. Zhao, Phase composition and valence of pulsed laser deposited vanadium oxide thin films at different oxygen pressures, Surf. Coat. Technol. 201 (2007) 5344–5347. doi:10.1016/j.surfcoat.2006.07.087.

[37] H. Liu, O. Vasquez, V.R. Santiago, L. Diaz, A.J. Rua, F.E. Fernandez, Novel pulsed-laser-deposition–VO_2 thin films for ultrafast applications, J. Electron. Mater. 34 (2005) 491–496. doi:10.1007/s11664-005-0056-y.

[38] X. Xu, A. Yin, X. Du, J. Wang, J. Liu, X. He, A novel sputtering oxidation coupling (SOC) method to fabricate VO_2 thin film, Appl. Surf. Sci. 256 (2010) 2750–2753. doi:10.1016/j.apsusc.2009.11.022.

[39] P. Ashok, Y.S. Chauhan, A. Verma, Vanadium dioxide thin films synthesized using low thermal budget atmospheric oxidation, Thin Solid Films. 706 (2020) 138003. doi:10.1016/j.tsf.2020.138003.

[40] P. Ashok, Y.S. Chauhan, A. Verma, Effect of vanadium thickness and deposition temperature on VO_2 synthesis using atmospheric pressure thermal oxidation, Thin Solid Films. 724 (2021) 138630. doi:10.1016/j.tsf.2021.138630.

[41] A.C. García-Wong, D. Pilloud, S. Bruyère, S. Mathieu, S. Migot, J.F. Pierson, F. Capon, Oxidation of sputter-deposited vanadium nitride as a new precursor to achieve thermochromic VO_2 thin films, Sol. Energy Mater. Sol. Cells. 210 (2020)

110474. doi:10.1016/j.solmat.2020.110474.

[42] A.C. García-Wong, D. Pilloud, S. Bruyère, D. Mangin, S. Migot, J.F. Pierson, F. Capon, Surface morphology-optical properties relationship in thermochromic VO_2 thin films obtained by air oxidation of vanadium nitride, J Materiomics. 7 (2021) 657–664. doi:10.1016/j.jmat.2020.12.005.

[43] A.J. Santos, B. Lacroix, M. Domínguez, R. García, N. Martin, F.M. Morales, Controlled grain-size thermochromic VO_2 coatings by the fast oxidation of sputtered vanadium or vanadium oxide films deposited at glancing angles, Surf. Interfaces. 27 (2021) 101581. doi:10.1016/j.surfin.2021.101581.

[44] A.J. Santos, B. Lacroix, F. Maudet, A. Corvisier, F. Paumier, C. Dupeyrat, T. Girardeau, R. García, F.M. Morales, Surface oxidation of amorphous Si and Ge slanted columnar and mesoporous thin films: Evidence, scrutiny and limitations for infrared optics, Appl. Surf. Sci. 493 (2019) 807–817. doi:10.1016/j.apsusc.2019.07.064.

[45] F.M. Morales, M. Escanciano, M.P. Yeste, A.J. Santos, Reactivity of vanadium nanoparticles with oxygen and tungsten, Nanomaterials. 12 (2022) 1471. doi:10.3390/nano12091471.

[46] A.J. Santos, M. Escanciano, A. Suárez-Llorens, M. Pilar Yeste, F.M. Morales, A novel route for the easy production of thermochromic VO_2 nanoparticles, Chem. - A Eur. J. 27 (2021) 16662–16669. doi:10.1002/chem.202102566.

[47] M.M. Hawkeye, M.J. Brett, Glancing angle deposition: Fabrication, properties, and applications of micro- and nanostructured thin films, J. Vac. Sci. Technol. A Vacuum, Surfaces, Film. 25 (2007) 1317. doi:10.1116/1.2764082.

[48] A. Barranco, A. Borras, A.R. Gonzalez-Elipe, A. Palmero, Perspectives on oblique angle deposition of thin films: From fundamentals to devices, Prog. Mater. Sci. 76 (2016) 59–153. doi:10.1016/j.pmatsci.2015.06.003.

[49] P. Shvets, O. Dikaya, K. Maksimova, A. Goikhman, A review of Raman spectroscopy of vanadium oxides, J. Raman Spectrosc. 50 (2019) 1226–1244. doi:10.1002/jrs.5616.

[50] A. Gloter, V. Serin, C. Turquat, C. Cesari, C. Leroux, G. Nihoul, Vanadium valency and hybridization in V-doped hafnia investigated by electron energy loss spectroscopy, Eur. Phys. J. B. 22 (2001) 179–186. doi:10.1007/PL00011142.

[51] D.S. Su, M. Wieske, E. Beckmann, A. Blume, G. Mestl, R. Schlögl, Electron beam induced reduction of V_2O_5 studied by analytical electron microscopy, Catal. Letters. 75 (2001) 81–86. doi:10.1023/A:1016754922933.

[52] J. Li, B.D. Gauntt, J. Kulik, E.C. Dickey, Stoichiometry of nanocrystalline VO_X thin films determined by electron energy loss spectroscopy, Microsc. Microanal. 15 (2009) 1004–1005. doi:10.1017/S1431927609092770.

[53] D. Singh, B. Viswanath, In situ nanomechanical behaviour of coexisting insulating and metallic domains in VO_2 microbeams, J. Mater. Sci. 52 (2017) 5589–5599. doi:10.1007/s10853-017-0792-4.

[54] M. Ertas Uslu, I.B. Misirlioglu, K. Sendur, Crossover of spectral reflectance lineshapes in Ge-doped VO_2 thin films, Opt. Mater. 104 (2020) 109890. doi:10.1016/j.optmat.2020.109890.

[55] E.E. Antunez, U. Salazar-Kuri, J.O. Estevez, J. Campos, M.A. Basurto, S.

Jiménez Sandoval, V. Agarwal, Porous silicon-VO_2 based hybrids as possible optical temperature sensor: Wavelength-dependent optical switching from visible to near-infrared range, J. Appl. Phys. 118 (2015) 134503. doi:10.1063/1.4932023.

[56] D. Fu, K. Liu, T. Tao, K. Lo, C. Cheng, B. Liu, R. Zhang, H.A. Bechtel, J. Wu, Comprehensive study of the metal-insulator transition in pulsed laser deposited epitaxial VO_2 thin films, J. Appl. Phys. 113 (2013) 043707. doi:10.1063/1.4788804.

[57] S. Kumar, F. Maury, N. Bahlawane, Electrical switching in semiconductor-metal self-assembled VO_2 disordered metamaterial coatings, Sci. Rep. 6 (2016) 37699. doi:10.1038/srep37699.

[58] C. Wan, Z. Zhang, D. Woolf, C.M. Hessel, J. Rensberg, J.M. Hensley, Y. Xiao, A. Shahsafi, J. Salman, S. Richter, Y. Sun, M.M. Qazilbash, R. Schmidt-Grund, C. Ronning, S. Ramanathan, M.A. Kats, On the optical properties of thin-film vanadium dioxide from the visible to the far infrared, Ann. Phys. 531 (2019) 1900188. doi:10.1002/andp.201900188.

[59] Q. Wang, M. Brier, S. Joshi, A. Puntambekar, V. Chakrapani, Defect-induced Burstein-Moss shift in reduced V_2O_5 nanostructures, Phys. Rev. B. 94 (2016) 245305. doi:10.1103/PhysRevB.94.245305.

[60] Z.M. Gibbs, A. Lalonde, G.J. Snyder, Optical band gap and the Burstein-Moss effect in iodine doped PbTe using diffuse reflectance infrared Fourier transform spectroscopy, New J. Phys. 15 (2013) 075020. doi:10.1088/1367-2630/15/7/075020.

[61] C. Zhang, O. Gunes, S. Wen, Q. Yang, S. Kasap, Effect of substrate temperature on the structural, optical and electrical properties of DC magnetron sputtered VO_2 Thin Films, Materials. 15 (2022) 7849. doi:10.3390/ma15217849.

[62] S. Chen, J. Liu, L. Wang, H. Luo, Y. Gao, Unraveling mechanism on reducing thermal hysteresis width of VO_2 by Ti doping: A joint experimental and theoretical study, J. Phys. Chem. C. 118 (2014) 18938−18944. doi:10.1021/jp5056842.

[63] R. Lopez, L.A. Boatner, T.E. Haynes, Enhanced hysteresis in the semiconductor-to-metal phase transition of VO_2 precipitates formed in SiO_2 by ion implantation, Appl. Phys. Lett. 79 (2001) 3161–3163. doi:10.1063/1.1415768.

[64] Y. Yang, X. Cao, G. Sun, S. Long, T. Chang, X. Li, Transmittance change with thickness for polycrystalline VO_2 films deposited at room temperature, J. Alloys Compd. 791 (2019) 648–654. doi:10.1016/j.jallcom.2019.03.278.

[65] M. Yethiraj, Pure and doped vanadium sesquioxide: A brief experimental review, J. Solid State Chem. 88 (1990) 53–69. doi:10.1016/0022-4596(90)90205-C.

[66] K. Kawashima, Y. Ueda, K. Kosuge, S. Kachi, Crystal growth and some electric properties of V_6O_{13}, J. Cryst. Growth. 26 (1974) 321–322. doi:10.1016/0022-0248(74)90265-6.

[67] A.L. Pergament, O.Y. Berezina, S. V. Burdyukh, V.P. Zlomanov, E.A. Tutov, Thin films of nanocrystalline vanadium dioxide: Modification of the properties, and electrical switching, Key Eng. Mater. 854 (2020) 103–108. doi:10.4028/www.scientific.net/KEM.854.103.

[68] C. Ling, Z. Zhao, X. Hu, J. Li, X. Zhao, Z. Wang, Y. Zhao, H. Jin, W Doping and voltage driven metal-insulator transition in VO_2 nano-films for smart switching devices, ACS Appl. Nano Mater. 2 (2019) 6738–6746. doi:10.1021/acsanm.9b01640.

[69] S. Cheng, M.H. Lee, X. Li, L. Fratino, F. Tesler, M.G. Han, J. del Valle, R.C. Dynes, M.J. Rozenberg, I.K. Schuller, Y. Zhu, Operando characterization of conductive filaments during resistive switching in Mott VO_2, Proc. Natl. Acad. Sci. U.S.A. 118 (2021) e2013676118. doi:10.1073/pnas.2013676118.

[70] I.H. Hwang, Y. Park, J.M. Choi, S.W. Han, Direct comparison of the electrical, optical, and structural phase transitions of VO_2 on ZnO nanostructures, Curr. Appl. Phys. 36 (2022) 1–8. doi:10.1016/j.cap.2021.12.016.

[71] V. Eyert, The metal-insulator transitions of VO_2: A band theoretical approach, Ann. Der Phys. 11 (2002) 650–704. doi: 10.1002/andp.20025140902.

[72] J.B. Goodenough, The two components of the crystallographic transition in VO_2, J. Solid State Chem. 3 (1971) 490–500. doi:10.1016/0022-4596(71)90091-0.

[73] A.J. Santos, N. Martin, J. Outón, E. Blanco, R. García, F.M. Morales, Towards the optimization of a simple route for the fabrication of energy-efficient VO_2-based smart coatings, Sol. Energy Mater. Sol. Cells. 254 (2023) 112253. doi:10.1016/j.solmat.2023.112253.

[74] A.J. Santos, N. Martin, J. Outón, E. Blanco, R. García, F.M. Morales, A simple two-step approach to the manufacture of VO_2-based coatings with unique thermochromic features for energy-efficient smart glazing, Energy Build. 285 (2023) 112892. doi:10.1016/j.enbuild.2023.112892.

[75] S. Yu, S. Wang, M. Lu, L. Zuo, A metal-insulator transition study of VO_2 thin films grown on sapphire substrates, J. Appl. Phys. 122 (2017) 235102. doi:10.1063/1.4997437.

[76] A. Gupta, R. Aggarwal, P. Gupta, T. Dutta, R.J. Narayan, J. Narayan, Semiconductor to metal transition characteristics of VO_2 thin films grown epitaxially on Si (001), Appl. Phys. Lett. 95 (2009) 111915. doi:10.1063/1.3232241.

[77] L. Chen, X. Wang, D. Wan, Y. Cui, B. Liu, S. Shi, H. Luo, Y. Gao, Tuning the phase transition temperature, electrical and optical properties of VO_2 by oxygen nonstoichiometry: Insights from first-principles calculations, RSC Adv. 6 (2016) 73070–73082. doi:10.1039/c6ra09449j.

Facile fabrication of high-performance thermochromic VO_2-based films on Si for application in phase-change devices

A.J. Santos[a,b,c,*], N. Martin[c], J.J. Jiménez[a,b], R. Alcántara[a,d], S. Margueron[c], A. Casas-Acuña[a,b], R. García[a,b], F. M. Morales[a,b]

[a] *IMEYMAT: Institute of Research on Electron Microscopy and Materials of the University of Cádiz, E-11510, Puerto Real, Spain.*

[b] *Department of Materials Science and Metallurgic Engineering, and Inorganic Chemistry, Faculty of Sciences, University of Cádiz, E-11510 Puerto Real, Spain.*

[c] *Université de Franche-Comté, CNRS, Institut FEMTO-ST, F-25000 Besançon, France.*

[d] *Department of Physical Chemistry, Faculty of Sciences, University of Cádiz, E-11510 Puerto Real, Spain.*

* Corresponding author: antonio.santos@uca.es

Abstract: This work reports on an alternative and advantageous procedure to attain VO_2-based thermochromic coatings on silicon substrates which involves the sputtering of vanadium thin films at glancing angles and their subsequent fast annealing in air atmosphere. By adjusting the thickness/porosity of the vanadium films as well as the thermal treatment parameters, high VO_2(M) yields were achieved for 100, 200 and 300 nm thick layers treated at 475 and 550°C for reaction times below 120 s. Comprehensive structural and compositional characterizations by Raman spectroscopy, X-ray diffraction and scanning-transmission electron microscopies combined with analytical techniques such as electron energy-loss spectroscopy allowed to evidence the successful synthesis of VO_2(M) + V_2O_3/V_6O_{13}/V_2O_5 mixtures. Likewise, a 200 nm thick coating consisting exclusively of VO_2(M) was also achieved. Conversely, the functional characterization of these samples was addressed by variable temperature spectral reflectance and resistivity measurements. The best results were obtained for the VO_2/Si sample, which experienced changes in reflectance of 30–65% in the near-infrared at temperatures between 25ºC and 110ºC. Similarly, it was also proven that the achieved mixtures of vanadium oxides can be advantageous for certain optical applications in specific infrared windows. Finally, the features of the different structural, optical and electrical hysteresis loops associated with the metal-insulator transition of the VO_2/Si sample were disclosed and compared. The remarkable thermochromic performances hereby accomplished highlight the suitability of these VO_2-based coatings for applications in a wide range of optical, optoelectronic and/or electronic smart devices.

Keywords: VO_2 thin films; glancing angle deposition; rapid thermal annealing; metal-to-insulator transition; thermochromism; smart devices.

Supplementary Material

SECTION I: Vis-NIR reflectance spectra at 25ºC and 110ºC for samples annealed at 475ºC

This section contains the reflectance spectra of the VO_2 + V_2O_3 (sample T100_475_60) and VO_2 + V_6O_{13} (samples T200_475_90 and T300_475_120) mixtures attained at 475ºC which, for reasons related to the organization and arrangement of the figures, were not included in the manuscript.

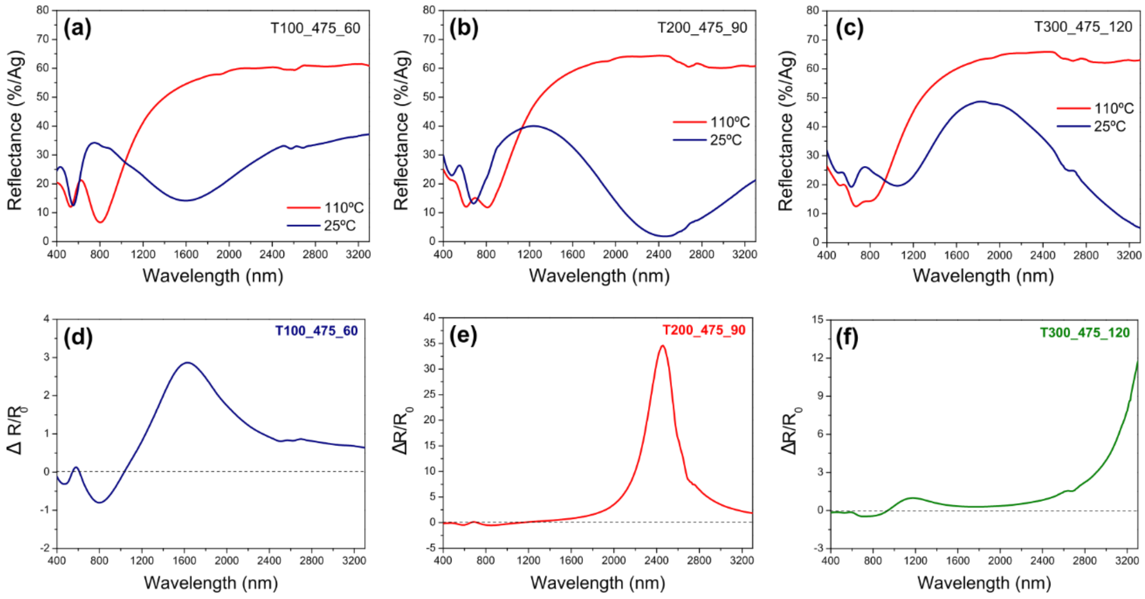

Fig. S1. Reflectance spectra recorded at 25ºC (blue) and 110ºC (red) for samples (a) T100_475_60, (b) T200_475_90 and (c) T300_475_120. Rate of change in reflectance $(R - R_0)/R_0$ at 25ºC (R_0) and 110ºC (R) for samples (d) T100_475_60, (e) T200_475_90 and (f) T300_475_120.

Table S1. Main features of the reflectance changes experienced by different annealed samples in the vis-NIR range when increasing temperature. ΔR_{max} indicates the maximum value taken by ΔR (which is given by the difference between the reflectance values at 110ºC and 25ºC, respectively); λ_{max} is the wavelength at which ΔR_{max} occurs; and λ_0 denotes the limiting wavelength beyond which ΔR only takes positive values.

Sample	**ΔR_{max} (%)**	**λ_{max} (nm)**	**λ_0 (nm)**
T100_475_60	40.8	1630	1035
T200_475_90	62.5	2460	1130
T300_475_120	58.0	3300	940

SECTION II: Electronic features of the MIT for VO_2 + V_6O_{13} mixtures

Fig. S2 shows the hysteresis loops for samples T200_475_90, T300_475_120 and T300_550_45 through resistivity *vs.* temperature measurements. Note that, despite the limited resistivity drops recorded, it was possible to evaluate the features of the electrical MIT for VO_2 + V_6O_{13} mixtures. **Table S2** lists the transition temperatures (T_c) during heating and cooling cycles, which were calculated from the derivative curves of the resistivity *vs*. temperature plots (**Fig. S2**) by fitting them with a Gaussian function and considering the peaks as the temperature of the minima variation rates, along with the hysteresis loop width (W_H) given by T_c (heating) – T_c (cooling).

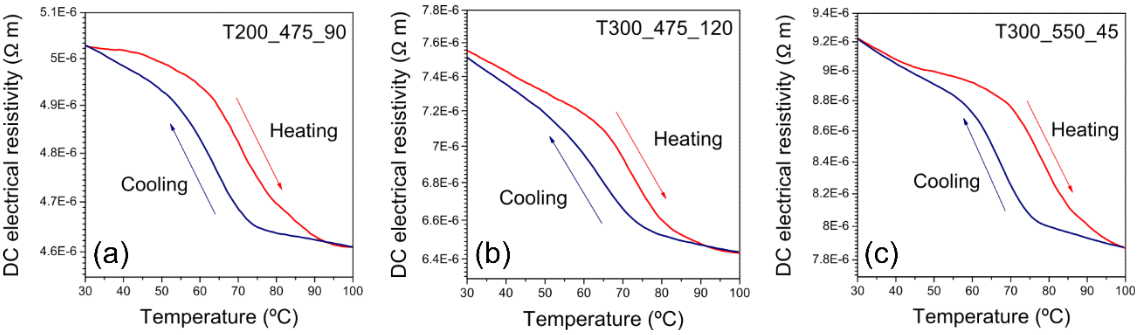

Fig. S2. Changes in DC electrical resistivity with temperature registered for samples (a) T200_475_90, (b) T300_475_120 and (c) T300_550_45 during heating (red) and cooling (blue) cycles.

Table S2. Main electronic features of the MIT extracted from the resistivity *vs*. temperature measurements carried out on VO_2 + V_6O_{13} mixtures.

Sample	**T_c (ºC) heating**	**T_c (ºC) cooling**	**W_H (ºC)**
T200_475_90	71	64	7
T300_475_120	72	64	8
T300_550_45	78	67	13